

1-1-2019

Effect of Si and C additions on the reaction mechanism and mechanical properties of FeCrNiCu high entropy alloy

Hao Wu

Sirui Huang

Huan Qiu

Heguo Zhu

Zonghan Xie

Edith Cowan University, z.xie@ecu.edu.au

Follow this and additional works at: <https://ro.ecu.edu.au/ecuworkspost2013>



Part of the [Engineering Commons](#)

10.1038/s41598-019-52809-y

Wu, H., Huang, S., Qiu, H., Zhu, H., & Xie, Z. (2019). Effect of Si and C additions on the reaction mechanism and mechanical properties of FeCrNiCu high entropy alloy. *Scientific Reports*, 9(1), Article 16356. Available [here](#)

This Journal Article is posted at Research Online.

<https://ro.ecu.edu.au/ecuworkspost2013/7204>

OPEN

Effect of Si and C additions on the reaction mechanism and mechanical properties of FeCrNiCu high entropy alloy

Hao Wu¹, Sirui Huang¹, Huan Qiu¹, Heguo Zhu^{1*} & Zonghan Xie^{2,3}

FeCrNiCu based high entropy alloy matrix composites were fabricated with addition of Si and C by vacuum electromagnetic induction melting. The primary goal of this research was to analyze the reaction mechanism, microstructure, mechanical properties at room temperature and strengthening mechanism of the composites with addition of Si and C. The reaction mechanism of powders containing (Si, Ni and C) was analyzed, only one reaction occurred (i.e., $\text{Si} + \text{C} \rightarrow \text{SiC}$) and its activation energy is 1302.8 kJ/mol. The new composites consist of a face centered cubic (FCC) structured matrix reinforced by submicron sized SiC particles. The addition of Si and C enhances the hardness from 351.4 HV to 626.4 HV and the tensile strength from 565.5 MPa to 846.0 MPa, accompanied by a slight decrease in the plasticity. The main strengthening mechanisms of SiC/FeCrNiCu composites were discussed based on dislocation strengthening, load bearing effect, Orowan mechanism and solid solution hardening, whose contributions to the tensile strength increase are 58.6%, 6.3%, 14.3% and 20.8%, respectively.

Traditionally, a small amount of alloying elements are often added into a base metal to improve the mechanical properties of the material. The resulting alloy is typically classified by the base element, such as ferrous or aluminum alloy. Different from traditional alloys, high entropy alloys (HEAs) consist of multiple principal elements^{1,2}. Instead of forming intermetallics, HEAs are single solid solutions made of face centered cubic (FCC)^{3,4}, body centered cubic (BCC)^{5,6} and hexagonal close-packed (HCP)⁷ or the mixture of them^{8,9}, manifest of the high mixing entropy and sluggish interdiffusion characteristic^{1,2,10}. HEAs have shown advantages of high thermodynamic stability¹¹, combination of high strength and ductility^{12–16}, good abrasive resistance^{17,18} and corrosion resistance¹⁹, suitable for applications involving harsh environment^{20–22}.

Ceramic particles have been used as reinforcement in high entropy alloy matrix composites, which have distinct properties with regard to the matrix. For example, AlZnMgCuZr lightweight high entropy alloy based composites were prepared by incorporating 10% of TiB₂²³; the compressive strength, hardness and elastic modulus of the composites were greatly enhanced due to the grain refinement. Lukasz *et al.*²⁴ prepared CoCrFeMnNi high entropy alloy matrix composites reinforced with Al₂O₃ nano-particles. Compared with CoCrFeMnNi matrix, the hardness of the composites increases from 418 HV to 515 HV, while the yield strength was enhanced by 35.6%.

In-situ composite, in which one or more enhancement phases are produced by chemical reactions, exhibit some unique advantages over *ex-situ* composites²⁵. For example, the reinforcement is uniformly distributed in the matrix and the reinforcement and the matrix is relatively stable with clean interface. So far, there have been a small number of researches on the production of high entropy alloy matrix composites reinforced with *ex-situ* SiC particles²⁶, but little report about composites reinforced with *in-situ* SiC particles. In this paper, HEA composites containing FeCrNiCu matrix and *in-situ* SiC particles were prepared by vacuum electromagnetic induction melting. The microstructure and mechanical properties of the composites were characterized and the strengthening mechanisms analyze.

¹College of Materials Science and Engineering, Nanjing University of Science and Technology, Nanjing, 210094, P.R. China. ²School of Mechanical Engineering, University of Adelaide, SA, 5005, Adelaide, Australia. ³School of Engineering, Edith Cowan University, WA, 6027, Joondalup, Australia. *email: zhg1200@sina.com

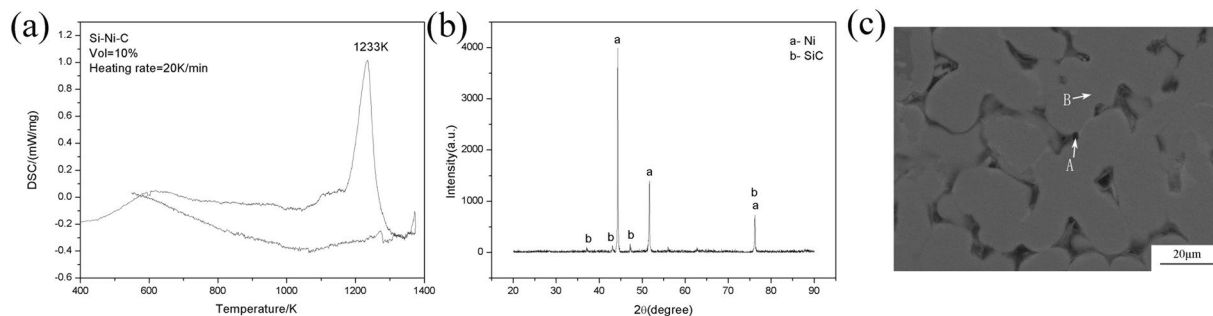


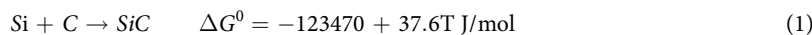
Figure 1. (a) DSC curve of Si-Ni-C system; (b) XRD diffraction pattern of Si-Ni-C system; (c) SEM image of Si-Ni-C system.

Figure	Area	Element	
		Ni	Si
Fig. 1c	A	28.53	71.47
	B	97.41	2.59

Table 1. Chemical compositions of different phases measured by SEM/EDS (areas marked in Fig. 1c).

Results and Discussion

DSC analysis. The DSC curve of the Si-C system (Fig. 1a) has a peak at 1233 K, signifying a reaction took place during the heating stage. The XRD diffraction pattern of the specimen prepared from heating up to 1300 K (Fig. 1b) shows the diffraction peaks of Ni and SiC^{27,28}. The SEM image (Fig. 1c) suggests the possible existence of Ni and SiC. The EDS analysis indicates that the gray region is made of Ni, while the dark region is composed of Si and C, which suggests the formation of SiC (Table 1) via:



The SC10 was taken as an example to determine the apparent activation energy of chemical reactions during materials synthesis. Figure 2 shows the DSC curve acquired at the heating rate of 15 K/min, 20 K/min, 25 K/min and 30 K/min, respectively. With the increase of the heating rate, the reaction peak became sharper and the reaction temperature was moving upward. According to Kissinger's equation²⁹, the activation energy, E , of the reaction can be defined as:

$$\frac{d\left(\ln \frac{\beta}{T_m^2}\right)}{d\left(\frac{1}{T_m}\right)} = -\frac{E}{R} \quad (2)$$

where T_m is the peak temperature of the reaction, β is the heating rate, and R is ideal gas constant (i.e., 8.31 J/mol). The peak temperature of the reactions at different heating rates (i.e. 15 K/min, 20 K/min, 25 K/min, and 30 K/min) can be obtained from Fig. 2. The relationship between $\ln(\beta/T_m^2) - 1/T_m$ can be plotted and fitted linearly through discrete points and the slope value is determined, which is -15.6767×10^4 (Fig. 3). The activation energy was calculated and found to be 1302.8 kJ/mol. The result shows that the formation of SiC requires a large amount of energy input and is thus difficult to form (at about 1233 K).

Microstructural characteristics. Figure 4a shows that XRD pattern of FeCrNiCu high entropy alloy matrix composites prepared with different additions of Si and C. The matrix is found to be FCC single phase solid solution. With the addition of Si and C, the diffraction peaks of SiC start to appear and becomes intensified with new SiC peak appearing at $2\theta \approx 61^\circ$, when the content of Si and C continues to increase. Compared with the base alloy, the FCC diffraction peaks of the composites is shifted to the left, presumably due to the lattice distortion caused by incorporation of Si and C. Figure 4b presents the enlarged diffraction pattern of the SC10, revealing the presence of the SiC particles with a FCC structure.

It can be seen from Fig. 5 that compared with the base alloy, the SiC reinforced composites exhibit drastic changes. In Fig. 5a, FeCrNiCu HEA has a homogeneous microstructure. With the addition of Si and C, SiC particles appear and are distributed uniformly in the matrix (Fig. 5b,c). The size of SiC particles was measured and found to be about 0.66 μm . The reinforcement content was analyzed using Image J software. In SC05 and SC10, the content of SiC is 3.5% and 6.4%, respectively.

Table 2 shows the matrix composition of the samples. Cu-rich and Cu-poor regions can be identified. Formation of these distinct regions may be explained by the ΔH_{mix} value between Cu and other atoms. The ΔH_{mix} values of Cu-Cr, Cu-Fe and Cu-Ni are 12 kJ/mol, 13 kJ/mol and 4 kJ/mol, respectively³⁰. The ΔH_{mix} value of

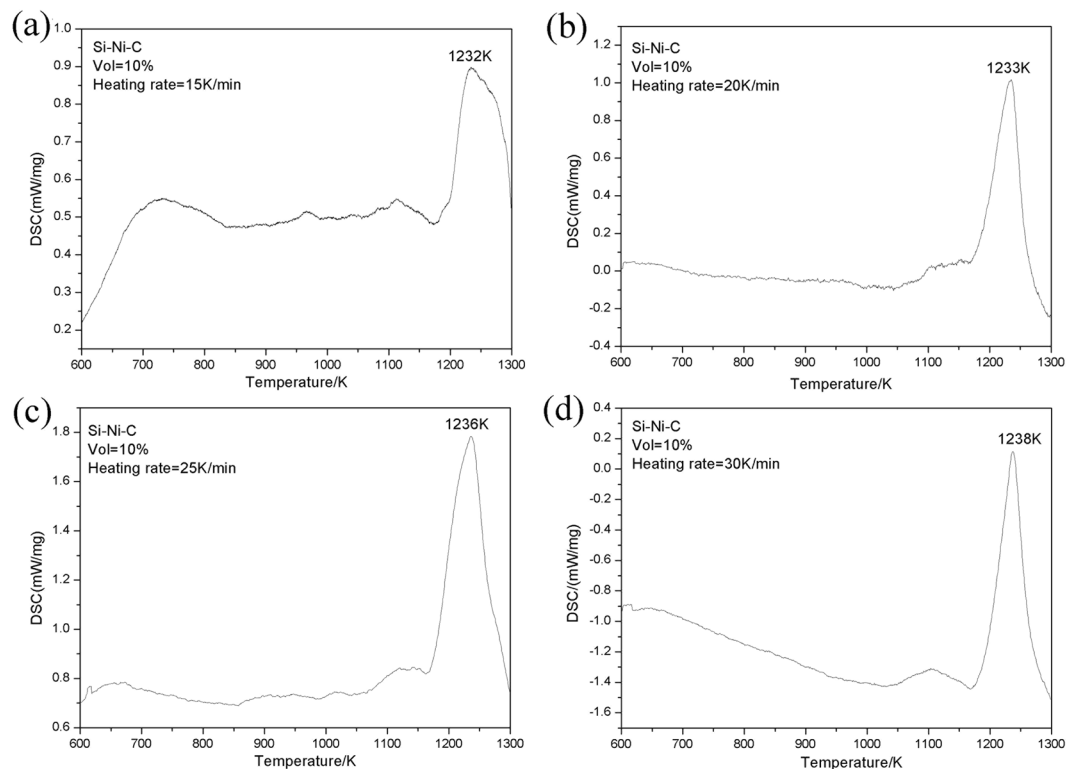


Figure 2. DSC curves obtained at four different heating rates, (a) 15 K/min; (b) 20 K/min; (c) 25 K/min; (d) 30 K/min.

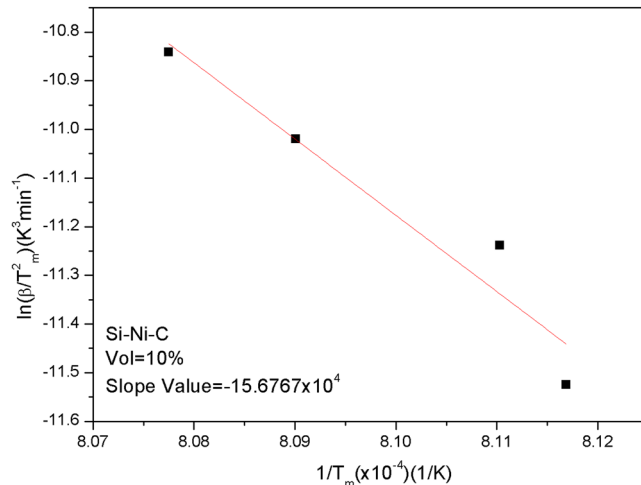


Figure 3. Plots of the $\ln(\beta/T_m^2) - 1/T_m$ for the reactions of Eq. (1).

Cu-Ni represents the lowest. With the formation of SiC particles, large congregations of Cu were becoming more apparent.

Figure 6 shows the detailed microstructure of SC00 alloy and SC10 composite. SiC particles have a circular shape. The selected area diffraction (SAED) pattern acquired from the matrix also confirm the FCC structure in the matrix. The diffraction pattern of the SiC particles is presented, along with the corresponding crystal plane exponents and lattice constants.

Mechanical properties. The engineering stress-strain curves of the FeCrNiCu matrix composites with different volume fractions of SiC at room temperature are displayed in Fig. 7. For comparison purposes, Table 3 lists the mechanical properties of these composites. The FeCrNiCu HEA shows high ductility with the plastic strain reaching 21.5%, while the tensile strength and hardness of the base alloy are only 565.5 MPa and 351.4 HV,

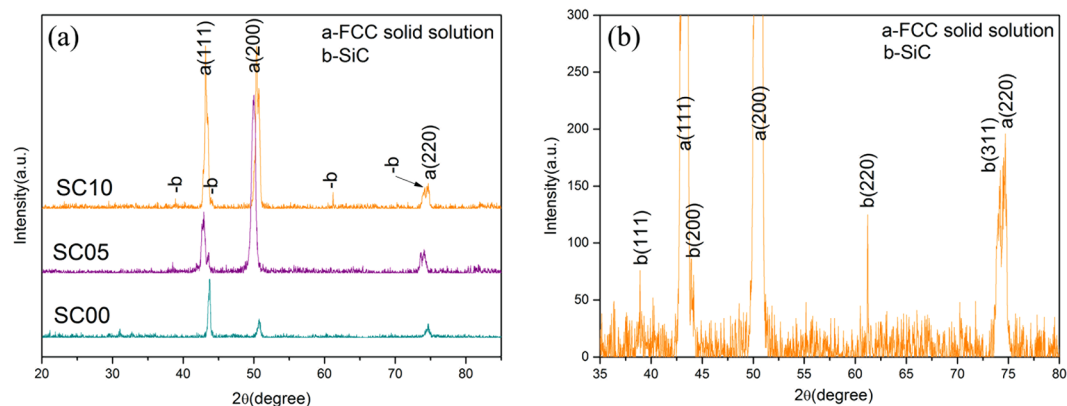


Figure 4. (a) XRD diffraction patterns of FeCrNiCu high entropy alloy matrix composites with different volumes of reinforcement agents; (b) Enlarged patterns of the HEA with 10% vol.SiC.

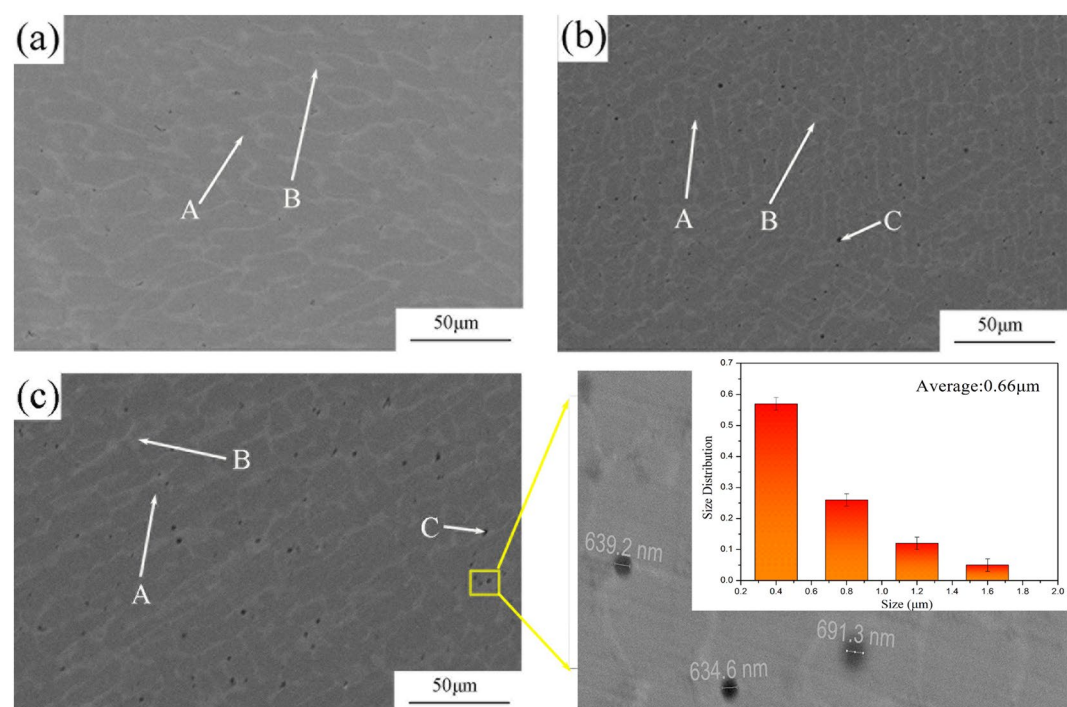


Figure 5. (a) SEM micrograph of FeCrNiCu high entropy alloy; (b) SEM micrograph of 5. vol% SiC/FeCrNiCu high entropy alloy matrix composite; (c) SEM micrograph of 10. vol% SiC/FeCrNiCu high entropy alloy matrix composite.

Specimen	Area	Element (at.%)				
		Fe	Cr	Ni	Cu	Si
SC00	A	30.90	29.95	27.17	11.98	—
	B	10.77	11.98	14.29	62.96	—
SC05	A	28.13	27.87	24.33	18.70	0.97
	B	9.48	7.52	19.14	62.59	1.26
	C	17.16	16.41	15.97	32.78	17.68
SC10	A	33.34	26.02	27.93	11.64	1.06
	B	8.19	7.08	12.41	70.75	1.57
	C	14.25	14.51	13.08	26.30	31.85

Table 2. Chemical compositions of different phases in the FeCrNiCu HEA and its composites by SEM/EDS (areas marked in Fig. 5).

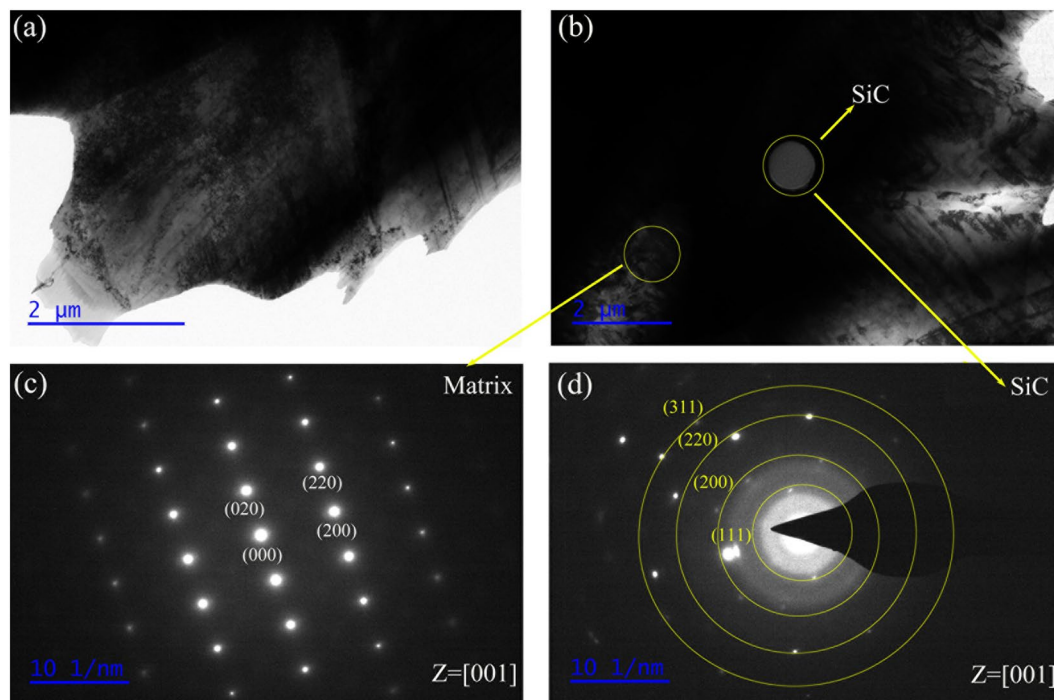


Figure 6. (a) TEM micrograph of FeCrNiCu high entropy alloy; (b) TEM micrograph of 10. vol% SiC/ FeCrNiCu high entropy alloy matrix composite; (c) the SAED of the FeCrNiCu matrix; (d) the SAED of the SiC particles.

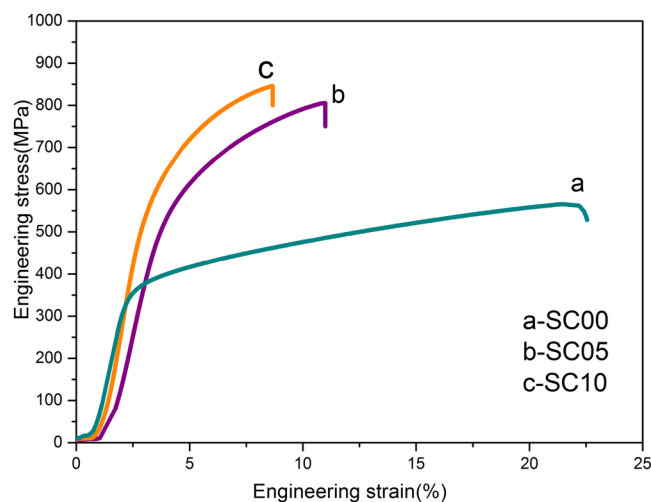


Figure 7. Engineering stress-strain curves of HEAs with different volume fractions of reinforcements.

Sample	σ_E /MPa	ϵ_E /%	HV
SC00	565.5	21.5	351.4
SC05	805.6	11.0	601.6
SC10	846.0	8.7	626.4

Table 3. Mechanical properties of the FeCrNiCu high entropy alloy with different volume fractions of SiC.

respectively. In comparison, the FeCrNiCu composites show a marked enhancement in hardness up to 626.4 HV. The tensile strength also increases from 565.5 MPa to 846.0 MPa (representing a 49.6% increase), accompanied by a decrease in ductility (i.e., 8.7%).

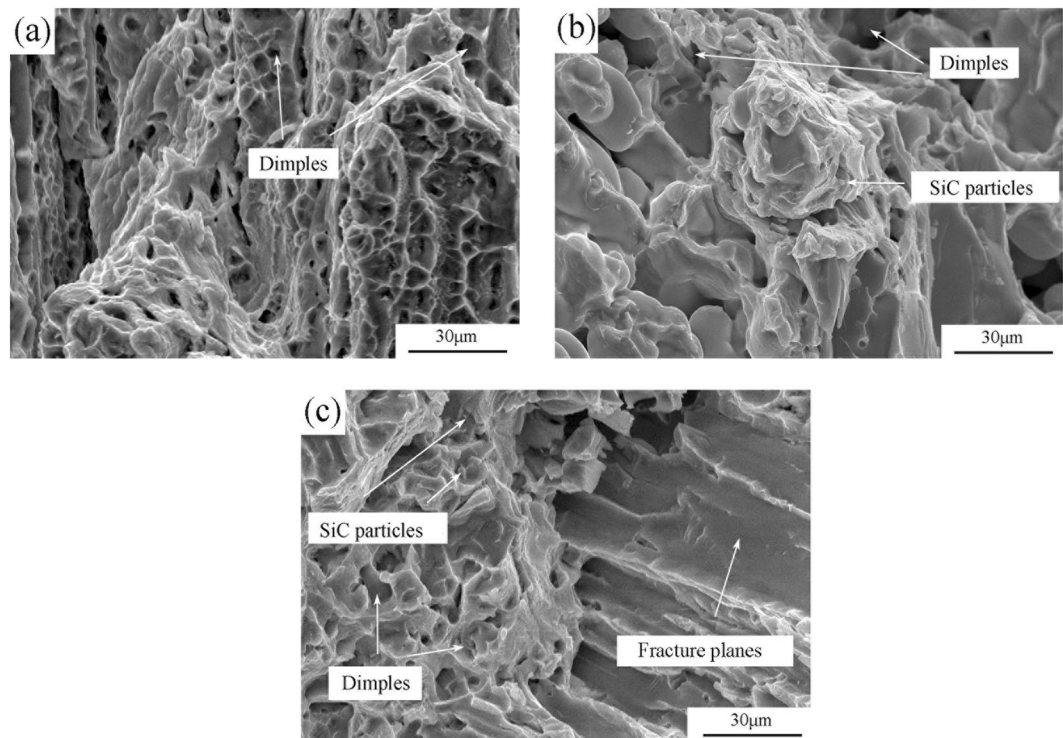


Figure 8. Fracture morphology of HEAs with different volume fractions of reinforcements, (a) matrix; (b) 5%; (c) 10%.

Fracture morphology. The tensile fracture surfaces of base alloy exhibit a large amount of small dimples (Fig. 8a), revealing ductile fracture pattern. Intact SiC particles are observed within the dimples (Fig. 8b), suggesting a strong interface bonding between the SiC particles and high entropy alloy matrix. When the volume fraction of SiC is 10%, the fracture morphology of the composite materials is shown in Fig. 8c. Small dimples and brittle fracture planes co-existed, revealing that the fracture was controlled by a mix of ductile and brittle processes. This resulted in a decline in material ductility. The above results are consistent with Table 3.

Strengthening mechanisms. The design of metal matrix composite is governed by the principle that the applied load can be transmitted to the reinforcement agents which are the main undertaker of the load³¹. The high density dislocations formed in the matrix material during synthesis also play an important role in strengthening the metal matrix composites³². Ramakrishnan *et al.* combined the role of the load-bearing effect and the dislocation strengthening mechanism in understanding the origin of a composite's strength³³. A composite model consists of three distinctive components; that is, elastic reinforcements, surrounding matrix-plastic zones and peripheral elastic areas, as exhibited in Fig. 9. Assuming that the plastic zone is governed by the ideal plastic state and the volume is constant. The rheological stress can be described by Mises's effective stress. The external boundary conditions are regulated by free radial stress. The radial stress and the shear strain are continuous in the matrix-plastic and matrix-elastic zones as the same as at the particle-matrix interface. The Mises's effective stress is continuous across the interface between matrix-plastic zone and matrix-elastic zone. The tensile strength of composites can be expressed as:

$$\sigma_{cy} = \sigma_y \times (1 + f_l)(1 + f_d) \quad (3)$$

where σ_{cy} and σ_y are the tensile strengths of the SC10 composite and SC00 alloy, respectively; f_l and f_d are the correction factor of load-bearing effect and the dislocation strength, respectively. The f_l and f_d can be defined as follows:

$$f_l = 0.5V_p \quad (4)$$

$$f_d = \frac{kG_m b \rho^{\frac{1}{2}}}{\sigma_y} \quad (5)$$

where V_p is the volume fraction of reinforced particles (~6.4%), k is a coefficient (~1.6), G_m is the shear modulus of the matrix (~102.4 GPa), b is the Burger vector (~0.286 nm²³) and the dislocated density ρ can be calculated by the equation below:

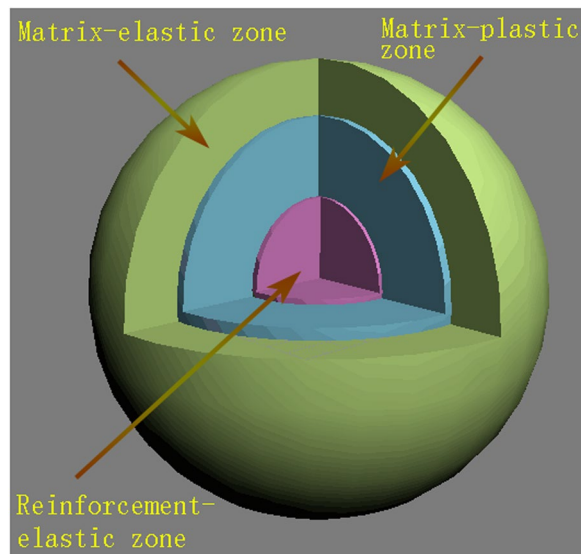


Figure 9. Sphere approximation of particles reinforced matrix composites.

$$\rho = \frac{9.6\Delta\alpha\Delta TV_p}{bd} \quad (6)$$

where $\Delta\alpha$ is the value of difference between the thermal expansion coefficients for the SiC reinforcement particles ($\sim 4.3 \times 10^{-6} \text{ K}^{-1}$ ³⁴) and the matrix (\sim approximately 0³⁵), ΔT is the value of difference between room temperature ($\sim 293 \text{ K}$) and processing temperature ($\sim 1233 \text{ K}$), V_p is the volume fraction of the reinforcements and d is the average size of SiC particles ($\sim 0.66 \mu\text{m}$).

Apart from the load-bearing effect and the dislocation strengthening, Orowan strengthening also contributes to the tensile strength of the composites. Orowan strengthening is generated by the interactions between dispersed reinforcements and dislocations. Accordingly, the tensile strength of the composites enhanced by *in-situ* SiC particles can be written as follows³⁶:

$$\Delta\sigma_O = \frac{0.13G_m b}{\lambda} \ln\left(\frac{d}{2b}\right) \quad (7)$$

where G_m is the shear modulus of the matrix, b is the Burger vector, d is the average size of SiC particles, and λ is the distance between the particles, which can be described as follows:

$$\lambda = d \left(\left(\frac{1}{2V_p} \right)^{\frac{1}{3}} - 1 \right) \quad (8)$$

where V_p is the volume fraction of *in-situ* SiC particles.

The solid solution strengthening is also one of important strengthening mechanisms. Solid solution strengthening is mainly realized by the uniform distribution of constituent atoms. When atoms are dissolved in the matrix to form solid solution, lattice distortion would occur in the matrix. The stress field caused by lattice distortion interacts with the stress field around the dislocations, which immobilizes the dislocations. As a result, the shear stress required for dislocation slip is increased in order to overcome the pinning effect. The rise of the tensile strength $\Delta\sigma_{\text{solute}}$ due to the solid solution strengthening can be expressed as³⁷:

$$\Delta\sigma_{\text{solute}} = MG \left(\frac{\varepsilon_{\text{SS}}^{\frac{3}{2}}}{700} \right) c^{\frac{1}{2}} \quad (9)$$

where M is the Taylor constant (~ 3.06 for FCC metals³⁸), G is the shear modulus of the matrix, c is the molar mass concentration of the solutes ($\sim 2.18 \text{ at. \%}$) and ε_{SS} is a coefficient associated with the fractional change in lattice coefficient per unit concentration of solute atom, which is in close connection with the atomic size of solutes³⁹. Count of $\varepsilon_{\text{SS}}^{3/2}/700$ for Si not reachable on account of the short of proper data. Because of the analogous atomic sizes, the date of $\varepsilon_{\text{SS}}^{3/2}/700$ is similar to 1.3×10^{-3} ³⁹. The ultimate tensile strength of the SC10 composite can be shown as:

$$\sigma_{\text{ey}} = \sigma_y \times (1 + f_l)(1 + f_d) + \Delta\sigma_O + \Delta\sigma_{\text{solute}} \quad (10)$$

The ideal or theoretical tensile strength can be calculated as:

$$\sigma_y = 565.5 \times (1 + 0.032) \times (1 + 0.30) + 41.30 + 60.14 = 860.11 \text{ MPa} \quad (11)$$

The highest contribution to the tensile strength thus came from the dislocation strengthening, which accounts for 58.6%. Three other contributions; i.e., the load bearing effect, Orowan strengthening and solid solution strengthening, account for 6.3%, 14.3% and 20.8%, respectively. The theoretical tensile strength of the composites (860.11 MPa) are in good agreement with experimental data (846.0 MPa). The small difference may be due to a small deviation in the size of SiC particles.

Conclusions

The *in-situ* composites containing of FeCrNiCu high entropy alloy matrix and SiC particles were designed and prepared by vacuum electromagnetic induction melting. The reaction process of the Si-Ni-C system consists of one step; i.e., Si reacting with C to form SiC particles as reinforcement phase. The activation energy of the reaction was found to be 1302.8 kJ/mol. The matrix of the as-sintered composites is mainly composed of Cu-rich phase and Cu-poor phase. The mechanical properties of the composites are significantly improved by the presence of SiC reinforcement phase. The hardness of SC10 is 78.3% higher than that of the matrix. The tensile strength of the composite is 846.0 MPa, which is 49.6% greater than that of the matrix. The multiple strengthening mechanisms were identified; namely, dislocation strengthening, load bearing effect, Orowan mechanism and solid solution strengthening. Among them the major contribution is from dislocation strengthening, which raised the tensile strength of the matrix by 58.6%.

Methods

Silicon powders (15–25 μm in radius), carbon powders (0.5–3 μm in radius), nickel powders (15–25 μm in radius), iron particles (0.5–1 mm in radius and 5 mm in length), copper particles (0.5–1 mm in radius and 5 mm in length) and chromium particle (0.5–1 mm in radius and 5 mm in length) were used as raw materials. Each of them has a purity of 99.9%. The volume fraction of Si and C in the high entropy alloy matrix composites was designed as 5% and 10%, respectively. Hence the resulting materials are designated as SC00 (Si and C-free), SC05 and SC10 composites, respectively. To begin with, the powders of Si, Ni and C were blended and ball-milled in a vacuum stainless steel jar under the speed of 250 rounds/min for 8 hours. Then the mixed powders were forged into small blocks under the pressure of 150 MPa at room temperature. The small blocks (containing Si, Ni and C) was further processed by high temperature sintering at 1373 K for 2 hours. The HEA composites were generated by vacuum electromagnetic induction melting. The three elemental particles (Fe, Cr and Cu) and prefabricated blocks were placed in a ceramic crucible inside an oven prior to induction melting. The vacuum level of the oven was reduced to 5×10^{-3} Pa by the mechanical and molecular pumps. The current was set to be 550 A, which was reduced to 300 A for electromagnetic stirring after the materials were fused. The molten metal was poured into a copper crucible and cooled to room temperature inside the furnace.

The green compact samples made from Si, Ni and C powders (each about 5–10 mg) were placed in a thermal analyzer (DSC, STA449C). The heating temperature was increased from the room temperature (293 K) to 1373 K at four different heating rates (i.e., 15 K/min, 20 K/min, 25 K/min and 30 K/min) before cooling down to 473 K at the rate of 30 K/min. Using four different types of DSC curve generated from these measurements, the apparent activation energy of the reaction system (Si-Ni-C) was calculated. The crystal structure of sintered materials including HEA composites was characterized by means of X-ray diffraction (XRD, Bruker-AXS D8 Advance) through the $\text{CuK}\alpha$ filtered ray scanning at a scanning speed of $4^\circ/\text{min}$. To observe the microstructure and tensile fracture morphology, a scanning electron microscope (SEM, Quant 250FEG) was used. The compositions of the HEA matrix composites were investigated by the energy-dispersive spectrometry (EDS, Quant 250FEG). ImageJ software was utilized to estimate the volume fractions of SiC particles for the two composites using the scanning electron microscope images obtained at $3000\times$ magnification; at least three SEM images were examined for each type of sample. The transmission electron microscopy (TEM, TECNAI G2 20 LaB6) was also used to further characterize the crystal structures and microstructures of the samples. The tensile tests were performed using a universal testing machine (UTM/CMT 5000) at a strain speed of 0.5 mm/min at room temperature. The tensile samples (length ~ 10.6 mm; width ~ 2.4 mm; and thickness ~ 1.2 mm) were wire cut from the ingots and then mechanically polished with emery paper to remove the surface defects. Vickers hardness tests were conducted using a hardness tester (HVS-1000). The maximum load was 5 N and the measurements were carried out in five different regions for each sample to ensure accuracy and confidence.

Received: 23 August 2019; Accepted: 21 October 2019;

Published online: 08 November 2019

References

1. Yeh, J. W. *et al.* Nanostructured high-entropy alloys with multiple principal elements: novel alloy design concepts and outcomes. *Adv. Eng. Mater.* **6**, 299–303 (2004).
2. Cantor, B., Chang, I. T. H., Knight, P. & Vincent, A. J. B. Microstructural development in equiatomic multicomponent alloys. *Mater. Sci. Eng. A* **375–377**, 213–218 (2004).
3. Eleti, R. R., Bhattacharjee, T., Zhao, L., Bhattacharjee, P. P. & Tsuji, N. Hot deformation behavior of cocrfemnni fcc high entropy alloy. *Mater. Chem. Phys.* **210**, 176–186 (2017).
4. Zhang, M. D. *et al.* Microstructure and enhanced mechanical behavior of the $\text{Al}_7\text{Co}_{24}\text{Cr}_{21}\text{Fe}_{24}\text{Ni}_{24}$ high-entropy alloy system by tuning the Cr content. *Mater. Sci. Eng. A* **733**, 299–306 (2018).
5. He, J. Y. *et al.* Effects of Al addition on structural evolution and tensile properties of the FeCoNiCrMn high-entropy alloy system. *Acta Mater.* **62**, 105–113 (2014).
6. Fan, J. T. *et al.* Improved the microstructure and mechanical properties of AlFeCoNi high-entropy alloy by carbon addition. *Mater. Sci. Eng. A* **728**, 30–39 (2018).

7. Gao, M. C., Zhang, B., Guo, S. M., Qiao, J. W. & Hawk, J. A. High-entropy alloys in hexagonal close-packed structure. *Metall. Mater. Trans. A* **47**(7), 3322–3332 (2016).
8. Gao, X. Z. *et al.* Microstructural origins of high strength and high ductility in an AlCoCrFeNi_{2.1} eutectic high-entropy alloy. *Acta Mater.* **141**, 59–66 (2017).
9. Basu, I., Ocelik, V. & Hosson, J. T. D. BCC-FCC interfacial effects on plasticity and strengthening mechanisms in high entropy alloys. *Acta Mater.* **157**, 83–95 (2018).
10. Yeh, J. W., Chen, Y. L., Lin, S. J. & Chen, S. K. High-entropy alloys—a new era of exploitation. *Mater. Sci. Forum* **560**, 1–9 (2007).
11. Santodonato, L. J. *et al.* Deviation from high-entropy configurations in the atomic distributions of a multi-principal-element alloy. *Nat. Commun.* **6**, 5964 (2015).
12. Tang, Q. H. *et al.* Hardening of an Al_{0.3}CoCrFeNi high entropy alloy via high-pressure torsion and thermal annealing. *Mater Lett* **151**, 126–129 (2015).
13. Cai, Y. P., Wang, G. J., Ma, Y. J., Cao, Z. H. & Meng, X. K. High hardness dual-phase high entropy alloy thin films produced by interface alloying. *Scr. Mater.* **162**, 281–285 (2019).
14. Zou, Y., Maiti, S., Steurer, W. & Spolenak, R. Size-dependent plasticity in an Nb₂₅Mo₂₅Ta₂₅W₂₅ refractory high-entropy alloy. *Acta Mater.* **65**, 85–97 (2014).
15. Gludovatz, B. *et al.* A fracture-resistant high-entropy alloy for cryogenic applications. *Science* **345**, 1153–1158 (2014).
16. Li, Z., Pradeep, K. G., Deng, Y., Raabe, D. & Tasan, C. C. Metastable high-entropy dual-phase alloys overcome the strength-ductility trade-off. *Nature* **534**, 227–230 (2016).
17. Chuang, M. H., Tsai, M. H., Wang, M. H., Lin, S. J. & Yeh, J. W. Microstructure and wear behavior of Al_{1.5}Co_{1.5}CrFeNi_{1.5}Ti_{1.5} high-entropy alloys. *Acta Mater.* **59**, 6308–6317 (2016).
18. Verma, A. *et al.* High temperature wear in CoCrFeNiCu high entropy alloys: The role of Cu. *Scr. Mater.* **161**, 28–31 (2019).
19. Zhang, X. R. *et al.* Influence of remelting and annealing treatment on corrosion resistance of AlFeNiCoCuCr high entropy alloy in 3.5% NaCl solution. *J. Alloys Compd.* **775**, 565–570 (2019).
20. Shafeie, S., Guo, S., Erhart, P., Hu, Q. & Palmqvist, A. Balancing Scattering Channels: A Panoscopic Approach toward Zero Temperature Coefficient of Resistance Using High-Entropy Alloys. *Adv. Mater.* **1805392**, 1–12 (2018).
21. Lu, Z. P. *et al.* An assessment on the future development of high-entropy alloys: summary from a recent workshop. *Intermetallics* **66**, 67–76 (2015).
22. Senkov, O. N., Miller, O. N., Miracle, D. B. & Woodward, C. Accelerated exploration of multi-principal element alloys with solid solution phases. *Nat. Commun.* **6**, 6529 (2015).
23. Li, H. *et al.* Microstructure and mechanical properties of an *in-situ* TiB₂/Al-Zn-Mg-Cu-Zr composite fabricated by Melt-SHS process. *Mater. Sci. Eng. A* **720**, 60–68 (2018).
24. Rogal, L., Kalita, L. & Lityńska-Dobrzynska, L. CoCrFeMnNi high entropy alloy matrix nanocomposite with addition of Al₂O₃. *Intermetallics* **86**, 104–109 (2017).
25. Shu, D. *et al.* *In situ* synthesized high volume fraction WC reinforced Ni-based coating by laser cladding. *Mater. Lett.* **195**, 178–181 (2017).
26. Rogal, L., Kalita, L., Tarasek, A., Bobrowski, P. & Czerwinski, P. Effect of SiC nano-particles on microstructure and mechanical properties of the CoCrFeMnNi high entropy alloy. *J. Alloys Compd.* **708**, 344–352 (2017).
27. Zhu, H. G. *et al.* Influences of carbon additions on reaction mechanisms and tensile properties of Al-based composites synthesized *in-situ* by Al-SiO₂ powder system. *Mater. Sci. Eng. A* **623**, 78–82 (2015).
28. Kasraee, K., Yousefpoura, M. & Tayebifard, S. A. Mechanical properties and microstructure of Ti₅Si₃ based composites prepared by combination of MASHS and SPS in Ti-Si-Ni and Ti-Si-Ni-C. *Systems. Mater. Chem. Phys.* **222**, 286–293 (2019).
29. Blaine, R. L. & Kissinger, H. E. Homer Kissinger and the Kissinger equation. *Thermochim. Acta* **540**(14), 1–6 (2012).
30. Takeuchi, A. & Inoue, A. Classification of Bulk Metallic Glasses by Atomic Size Difference, Heat of Mixing and Period of Constituent Elements and its Application to Characterization of the Main Alloying Element. *Mater. Trans.* **46**, 2817–2829 (2005).
31. Nardone, V. C. & Prewo, K. M. On the strength of discontinuous silicon carbide reinforced aluminum composites. *Scr. Metall.* **20**, 43–48 (1986).
32. Arsenault, R. J. & Shi, N. Dislocation generation due to differences between the coefficients of thermal expansion. *Mater. Sci. Eng.* **81**, 175–187 (1986).
33. Ramakrishnan, N. An analytical study on the strengthening of particulate reinforced metal matrix composites. *Acta mater* **44**, 69–77 (1996).
34. Zhang, X. Z. & Chen, T. J. Solution treatment: A route towards enhancing tensile ductility of SiCp/6061Al composite via powder thixoforming and comparison of micromechanical strength modeling. *Mater. Sci. Eng. A* **696**, 466–477 (2017).
35. Miracle, D. B. & Senkov, O. N. A critical review of high entropy alloys and related concepts. *Acta Mater.* **122**, 448–511 (2017).
36. Zhang, Z. & Chen, Z. Consideration of Orowan strengthening effect in particulate-reinforced metal matrix nanocomposites: A model for predicting their yield strength. *Scr. Mater.* **54**, 1321–1326 (2006).
37. Fu, Z. *et al.* Microstructure and strengthening mechanisms in an FCC structured single-phase nanocrystalline Co₂₅Ni₂₅Fe₂₅Al_{7.5}Cu_{17.5} high-entropy alloy. *Acta Mater.* **107**, 59–71 (2016).
38. Yim, D., Sathiyamoorthi, P., Hong, S. & Kim, H. S. Fabrication and mechanical properties of TiC reinforced CoCrFeMnNi high-entropy alloy composite by water atomization and spark plasma sintering. *J. Alloys Compd.* **781**, 389–396 (2019).
39. Song, R. K., Wei, L. J., Yang, C. X. & Wu, S. J. Phase formation and strengthening mechanisms in a dual-phase nanocrystalline CrMnFeVTi high-entropy alloy with ultrahigh hardness. *J. Alloys Compd.* **744**, 552–560 (2018).

Acknowledgements

This work was supported by the National Natural Science Foundation of China (No. 51571118, and No. 51371098) and the Natural Science Foundation of Jiangsu Province (No. BK20141308). Jiangsu Province Science and Technology Plan Project (BE2018753/KJ185629). Z. Xie acknowledges the support of the Australian Research Council Discovery Projects.

Author contributions

H.Z. designed experiments. H.W. contributed to the test and analysis experimental dates

Competing interests

The authors declare no competing interests.

Additional information

Correspondence and requests for materials should be addressed to H.Z.

Reprints and permissions information is available at www.nature.com/reprints.

Publisher's note Springer Nature remains neutral with regard to jurisdictional claims in published maps and institutional affiliations.



Open Access This article is licensed under a Creative Commons Attribution 4.0 International License, which permits use, sharing, adaptation, distribution and reproduction in any medium or format, as long as you give appropriate credit to the original author(s) and the source, provide a link to the Creative Commons license, and indicate if changes were made. The images or other third party material in this article are included in the article's Creative Commons license, unless indicated otherwise in a credit line to the material. If material is not included in the article's Creative Commons license and your intended use is not permitted by statutory regulation or exceeds the permitted use, you will need to obtain permission directly from the copyright holder. To view a copy of this license, visit <http://creativecommons.org/licenses/by/4.0/>.

© The Author(s) 2019